Title	Cascaded energy transfer and enhanced near-infrared emission in visible-pumped Cr and Nd co-doped Yb:YAG
Author(s)	Fujioka, Kana; Murakami, Taro; Motokoshi, Shinji et al.
Citation	Optical Materials. 2022, 128, p. 112396
Version Type	AM
URL	https://hdl.handle.net/11094/88502
rights	© 2022. This manuscript version is made available under the Creative Commons Attribution-NonCommercial-NoDerivatives 4.0 International License.
Note	

Cascaded energy transfer and enhanced near-infrared emission in visible-pumped Cr and Nd co-doped Yb:YAG

Kana Fujioka[a*], Taro Murakami[a], Shinji Motokoshi[b, a], Takagimi Yanagitani[c], Hidetsugu Yoshida[a], Koji Tsubakimoto[a], Kazuhisa Yamamoto[a], and Noriaki Miyanaga[b, a]

[a]*Institute of Laser Engineering, Osaka University, 2-6 Yamada-oka, Suita, Osaka 565-0871, Japan*

[b]*Institute for Laser Technology, 2-6 Yamada-oka, Suita, Osaka 565-0871, Japan*

[c]*Konoshima Chemical Co. Ltd., 80 Kouda, Takuma, Mitoyo-gun, Kagawa 769-1103, Japan*

[*]**Corresponding author**

Institute of Laser Engineering, Osaka University, 2-6 Yamada-oka, Suita, Osaka 565-0871, Japan

E-mail: fujioka-kana@ile.osaka-u.ac.jp

Abstract

In this study, the energy transfer mechanism in Cr,Nd,Yb:YAG (yttrium aluminum garnet) materials was investigated.

Based on the emission/excitation spectra and the temporal evolutions of the donor and acceptor ions in Cr,Nd:YAG, Nd,Yb:YAG, and Cr,Nd,Yb:YAG materials, the role of the cascaded $Cr^{3+} \rightarrow Nd^{3+} \rightarrow Yb^{3+}$ energy transfer was

elucidated in terms of Yb fluorescence enhancement. The quantum yield balance among Cr, Nd, and Yb

fluorescences was determined by solving rate equations, which utilized parameters such as the lifetimes of Cr^{3+}, Nd^{3+},

and Yb^{3+} ions and the energy transfer parameters related to these materials. The quantum yield for Yb fluorescence

was determined to be 35-81% at a Yb concentration of 1–7 at%.

Keywords: yttrium aluminum garnet, Yb-doped YAG, multiple doping, rare-earth, energy transport, cascaded energy

transport

Highlights:

- Cr,Nd,Yb:YAG powders were synthesized by the sol-gel method.

- The temporal evolutions of the donor and acceptor ions were measured.

- The energy transfer parameters were experimentally determined.

- The number densities of the excited Cr^{3+}, Nd^{3+}, and Yb^{3+} ions are discussed.

- The quantum yield balance among Cr, Nd, and Yb fluorescences was determined.

Abbreviations

energy transfer (ET): yttrium aluminum garnet (YAG): crystalline silicon photovoltaic (c-Si PV): inductively

coupled plasma spectroscopy (ICP): X-ray diffraction (XRD).

1. Introduction

Many studies have been conducted on the energy transfer (ET) in doubly doped yttrium aluminum garnet (YAG) materials in terms of the sensitization of emission in the near-infrared region. Cr and Nd co-doped YAG (hereafter abbreviated as Cr,Nd:YAG), for example, has been extensively studied for realizing solar-pumped lasers and improving the efficiency of lamp-pumped lasers [1, 2]. Nd^{3+} ions (trivalent rare-earth ion), with a 4f electron configuration, occupy the dodecahedral Y^{3+} sites in the YAG lattice. On the other hand, the majority of Cr^{3+} ions with 3d configurations occupy the octahedral Al^{3+} positions. The efficient ET from the excited Cr^{3+} ions to the Nd^{3+} ions occurs because the absorption spectrum of the acceptor (Nd^{3+} ions) is widely overlapped by the emission spectrum of the donor (Cr^{3+} ions). The efficiency of the Cr^{3+} to Nd^{3+} energy transfer (hereafter abbreviated as $Cr^{3+} \rightarrow Nd^{3+}$ ET) depends on temperature because of the thermal population distribution between the $^4T_2$ and ^2E states of Cr^{3+} ions [3–5]. Hong *et al*. showed that an electric dipole-dipole interaction was adequate for describing this ET process for temperatures up to ~400 K [6]. Lupei *et al*., on the other hand, quantitatively analyzed the de-excitation of the Cr^{3+} ions and excitation of the Nd^{3+} ions in Cr,Nd:YAG transparent ceramics using a theoretical model based on the dipole-dipole interaction approximation and found the Nd emission quantum efficiency to be 52% and 77% for 1-at% and 2-at% Nd concentration, respectively [7].

A similar ET mechanism for a different donor-acceptor combination was also demonstrated for Nd,Yb:YAG, showing that the efficiency of the $Nd^{3+} \rightarrow Yb^{3+}$ ET increased linearly up to ~83% with increasing Yb concentration [8]. For another dopant combination, Cr,Yb:YAG was found to improve the efficiency of crystalline silicon

photovoltaic (c-Si PV) cells [9]. The spectral sensitivity of c-Si PV is maximum at ~1000 nm because of the band

gap energy of Si (1.12 eV), and it decreases with decreasing light wavelength to ~1/3 of the maximum at ~400 nm.

The mechanism of the $Cr^{3+}(^2E$ state$) \rightarrow Yb^{3+}(^2F_{5/2}$ state$)$ r ET was thought to be a multi-phonon-assisted process, and

the estimated efficiency increased from ~15% at a Yb^{3+} concentration of 2 mol% to ~60% at a Yb^{3+} concentration of

10 mol%.

Several studies have been published on triply doped YAG materials to date. Ce,Cr,Nd:YAG materials with

a variety of combinations of Ce and Cr concentrations were investigated for improving the efficiency of solar-pumped

lasers, showing that Ce^{3+} ions act as effective sensitizers for Nd^{3+} ions [10]. As for Cr,Nd,Yb:YAG, Cr^{3+} ions can

sensitize the emission of Yb^{3+} ions via both $Cr^{3+} \rightarrow Nd^{3+} \rightarrow Yb^{3+}$ and $Cr^{3+} \rightarrow Yb^{3+}$ ETs [11]. However, the cascaded

process of the $Cr^{3+} \rightarrow Nd^{3+} \rightarrow Yb^{3+}$ energy transport is not well understood. The purpose of this study is to analyze

Cr,Nd,Yb:YAG materials using a database of emission/excitation spectra and the temporal evolutions of the donor

and acceptor ions for Cr,Nd:YAG, Nd,Yb:YAG, and Cr,Nd,Yb:YAG materials. Based on this database, the quantum

yield balance among Cr, Nd, and Yb fluorescences is estimated by solving rate equations that utilize the lifetimes of

Cr^{3+}, Nd^{3+}, and Yb^{3+} ions and the ET parameters related to these materials.

2. Fabrication and spectroscopic properties of Cr^{3+}, Nd^{3+} and Yb^{3+} co-doped YAG powders

2.1 Preparation of the sample powder

We fabricated the sample powders using the sol-gel method, which is suitable for pre-evaluating rare-earth ion-doped YAG materials [12]. The reagents used were a mixture of $Al(O\text{-}sec\text{-}C_4H_9)_3$ and $(CH_3)_2CHOH$ (97%), $Y(CH_3COO)_3 \cdot 4H_2O$ (yttrium acetate tetrahydrate, 99.99%), $Cr(CH_3COO)_3 \cdot xH_2O$ (chromium acetate hydrate), $Nd(CH_3COO)_3 \cdot H_2O$ (neodymium acetate monohydrate, 99.9%), $Yb(CH_3COO)_3 \cdot H_2O$ (ytterbium acetate monohydrate, 99.99%), and anhydrous 2-propanol. Furthermore, ultra-pure water with a resistivity of over 13 $M\Omega/cm$ was used. The concentration of each element in the fabricated powder was measured by inductively coupled plasma spectroscopy (ICP, Seiko Instruments Inc. SPS7800). The crystal phase of the fabricated powder with the anneal treatment at 1400˚C was identified by x-ray diffraction (XRD; Rigaku RINT2500). The measured diffraction patterns agreed well with those of the YAG crystal [13]. We did not observe peaks corresponding to the YAM ($Y_4Al_2O_9$) and YAP ($YAlO_3$) phases except for very weak peaks corresponding to the corundum Al_2O_3. The doping concentration (at%) is shown as the ratio of the number of exchanged Nd^{3+} or Yb^{3+} ions to that of Y^{3+} sites as well as the ratio of that of exchanged Cr^{3+} to the number of Al^{3+} sites. The maximum concentration of Cr^{3+} was fixed at 1 at% in order to avoid the deformation of the YAG crystal structure, and the concentration of Nd^{3+} was also set to be 1 at% to suppress concentration quenching [2], whereas the concentration of Yb^{3+} was changed in the range of 0–7 at%. Hereafter, the sample notations are defined such that the doping concentrations (C_{Cr}, C_{Nd}, and C_{Yb}) of $Cr(x),Nd(y),Yb(z)$:YAG correspond to $C_{Cr} = x$, $C_{Nd} = y$, and $C_{Yb} = z$ at% for Cr^{3+}, Nd^{3+}, and Yb^{3+} ions, respectively.

2.2 Excitation spectra of 1030-nm Yb fluorescence

Figure 1 shows a schematic illustration of the energy level diagrams of the Cr^{3+}, Nd^{3+}, and Yb^{3+} ions. Cr^{3+} ions are

photo-excited to the $^4T_1$ or $^4T_2$ state, and then they decay nonradiatively to the ^2E state. The inherent lifetime of the

^2E state is relatively long (8.8 ms) [6] because the transition from the ^2E state to the ground state $^4A_2$, which

corresponds to the R line fluorescence at a wavelength of 688 nm, is spin-forbidden. On the other hand, the ions in

the $^4T_2$ state rapidly relax to the ground state by emitting broad spectral fluorescence in the 600–850 nm wavelength

range. Because the energy difference ($\mathit{\Delta E}$) between ^2E and $^4T_2$ is as small as 700–800 cm^{-1}, these two states are

thermally coupled with the same lifetime of a few ms [5–7]. Nd^{3+} ions have many absorption bands corresponding

to the transitions from the ground state $^4I_{9/2}$ to $^4F_{3/2}$, $^4F_{5/2}$, and other higher excited states, and the fluorescence occurs

in the wavelength ranges of 850–950 nm ($^4F_{3/2} \rightarrow ^4I_{9/2}$ transition), 1050–1150 nm ($^4F_{3/2} \rightarrow ^4I_{11/2}$ transition), and 1300–

1400 nm ($^4F_{3/2} \rightarrow ^4I_{13/2}$ transition). The Yb^{3+} ion is a simple quasi-three-level system consisting of only two manifolds

($^2F_{7/2}$ and $^2F_{5/2}$), and the wavelength of the peak fluorescence intensity is approximately 1030 nm.
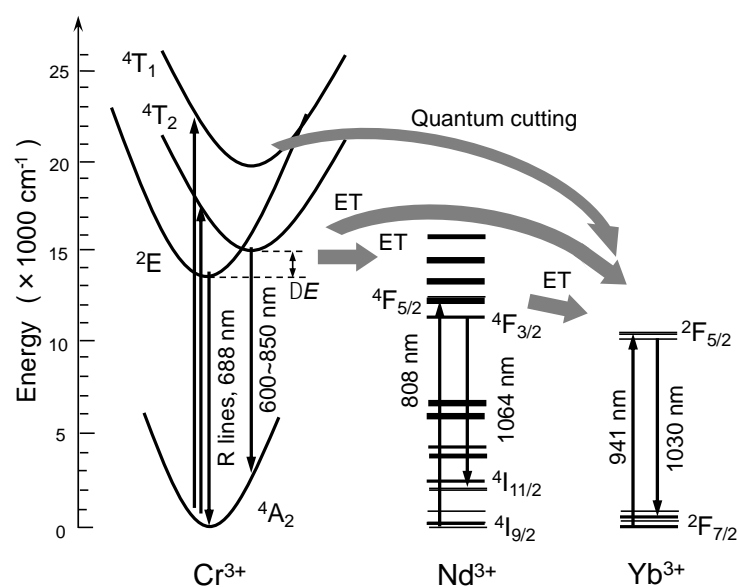
Fig. 1. Schematic illustration of the energy level diagrams of the Cr^{3+}, Nd^{3+} and Yb^{3+} ions. Thick arrows denote the possible energy transfer (ET) and the quantum cutting processes between the different ion species.

Among these three ions, the upper state energy of Cr^{3+} is the highest, followed by Nd^{3+} and Yb^{3+}. Therefore, one can hypothesize that the energy of the excited Cr^{3+} ions is transferred to the Nd^{3+} ions and/or Yb^{3+} ions, and the energy of the excited Nd^{3+} ions is transferred to the Yb^{3+} ions as schematically shown in Fig. 1. In addition to the Förster–Dexter energy transfer, the quantum cutting process may exist in the combination of Cr^{3+} and Yb^{3+}, since the bottom energy of the $^4T_1$ state of Cr^{3+} is almost twice as high as the $^2F_{5/2}$ state of Yb^{3+}. As a result, a large amount of energy absorbed by the Cr^{3+} ions is accumulated in the Yb^{3+} ions.

To examine this hypothesis, we measured the excitation spectra at 1030-nm fluorescence for Cr(1),Nd(0,1,3),Yb(1):YAG powders at room temperature using a high-resolution spectrophotometer (JASCO SS-

25), as shown in Fig. 2. Hereafter, all experiments were performed at room temperature. In the case of Cr,Yb:YAG,

the excitation spectral peaks around 940 nm and 970 nm correspond to the Yb^{3+} absorption band originating from the

$^2F_{7/2} \rightarrow {}^2F_{5/2}$ transition. It should be noted that the Yb absorption band coincides with the spectral gap due to absorption

by H_2O molecules in the solar spectrum (AM 1.5), as indicated by the dotted green line in Fig. 2. Therefore, Yb:YAG

does not degrade the efficiency of c-Si PV cells. The broad visible spectral bands around 450 nm and 600 nm, which

correspond to Cr^{3+}: $^4T_1$ and $^4T_2$ levels, respectively, significantly contribute to the Yb fluorescence. This observation

shows efficient ET from Cr^{3+} to Yb^{3+}. When Nd^{3+} ions were co-doped to Cr,Yb:YAG, the Nd absorption bands shown

in Fig. 2 also contributed to the Yb^{3+} fluorescence, in proportion to the Nd^{3+} concentration, suggesting that the energy

stored in the excited states of Nd^{3+} was efficiently transferred to Yb^{3+}. Moreover, the contribution of the Cr^{3+}: $^4T_2$

level to the Yb^{3+} fluorescence was enhanced by Nd^{3+}ions, which implied that a part of the energy stored in the $^4T_2$

level of Cr^{3+} was transferred to Yb^{3+} via Nd^{3+} excited states. As seen in Fig. 2, the excitation spectra of the Yb

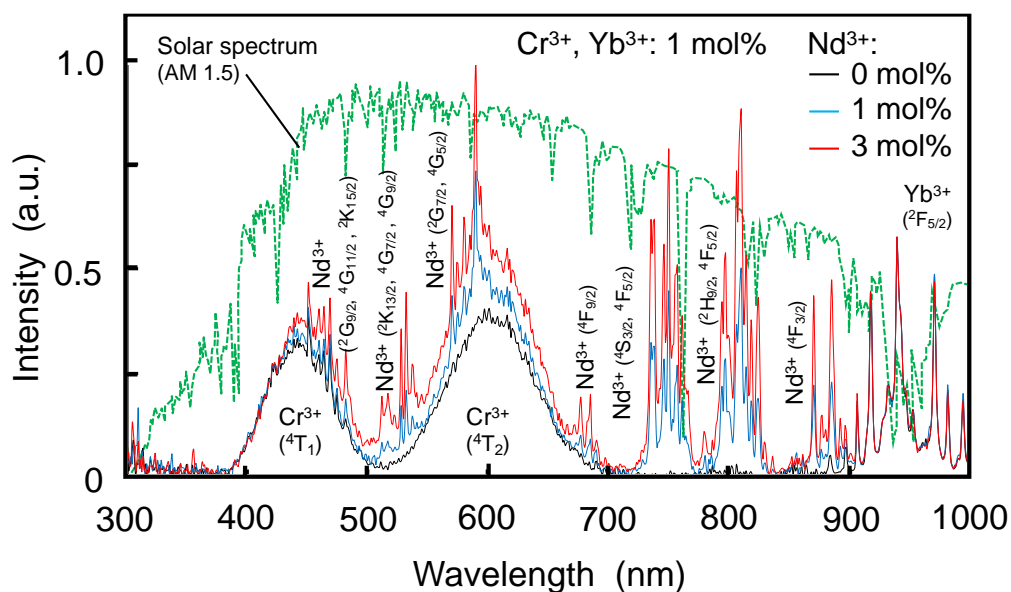fluorescence of Cr,Nd,Yb:YAG widely cover the solar spectrum, as expected.

Fig. 2. Excitation spectra of 1030-nm Yb emission for Cr,Yb:YAG powder (black line) and Cr,Nd,Yb:YAG powder

(blue and red lines). The solar spectrum (AM 1.5, dotted green line) is shown for reference.

2.3 Typical features of fluorescence with the excitation of Cr^{3+} ions

Hereafter, the doping concentration of Nd^{3+} ions was fixed at 1 at% to reduce concentration quenching [14]. To

understand the role of Cr^{3+} and Nd^{3+} ions in the mechanism of Yb^{3+} excitation, we measured the fluorescence spectra

of Cr(1):YAG, Cr(1),Nd(1):YAG, and Cr(1),Nd(1),Yb(1):YAG powders pumped at 440–450 nm. As shown in Fig.

3(a), the fluorescence spectrum of Cr^{3+} consisted of R lines at ~688 nm ($^2E \rightarrow ^4A_2$ transition), Stokes and anti-Stokes

components of vibrational (phonon-assisted) side bands, and a broad band due to the $^4T_2 \rightarrow ^4A_2$ transition. We

observed a line emission at 694 nm, which was most likely due to $Cr^{3+}:Al_2O_3$ phase resulting from the preferential

crystallization during the anneal treatment [15, 16]. The net energy content of the 694-nm line emission was not

significant (~3.2% of the total fluorescence energy) and did not contribute to the ET to the Nd^{3+} and/or Yb^{3+} ions.

This observation suggested the presence of localized $Cr^{3+}:Al_2O_3$ phase with a very low volume content. When Nd^{3+}

ions were added (Fig. 3 (b)), except for the 694-nm line emission, the intensity of Cr^{3+} fluorescence significantly

decreased owing to the $Cr^{3+} \rightarrow Nd^{3+}$ ET, resulting in the appearance of Nd fluorescence corresponding to the

transitions $^4F_{3/2} \rightarrow ^4I_{9/2}$ and $^4F_{3/2} \rightarrow ^4I_{11/2}$. Moreover, the Yb fluorescence became significant because of the direct

$Cr^{3+} \rightarrow Yb^{3+}$ ET and cascaded $Cr^{3+} \rightarrow Nd^{3+} \rightarrow Yb^{3+}$ ET in the Cr,Nd,Yb:YAG, as shown in Fig. 3(c).
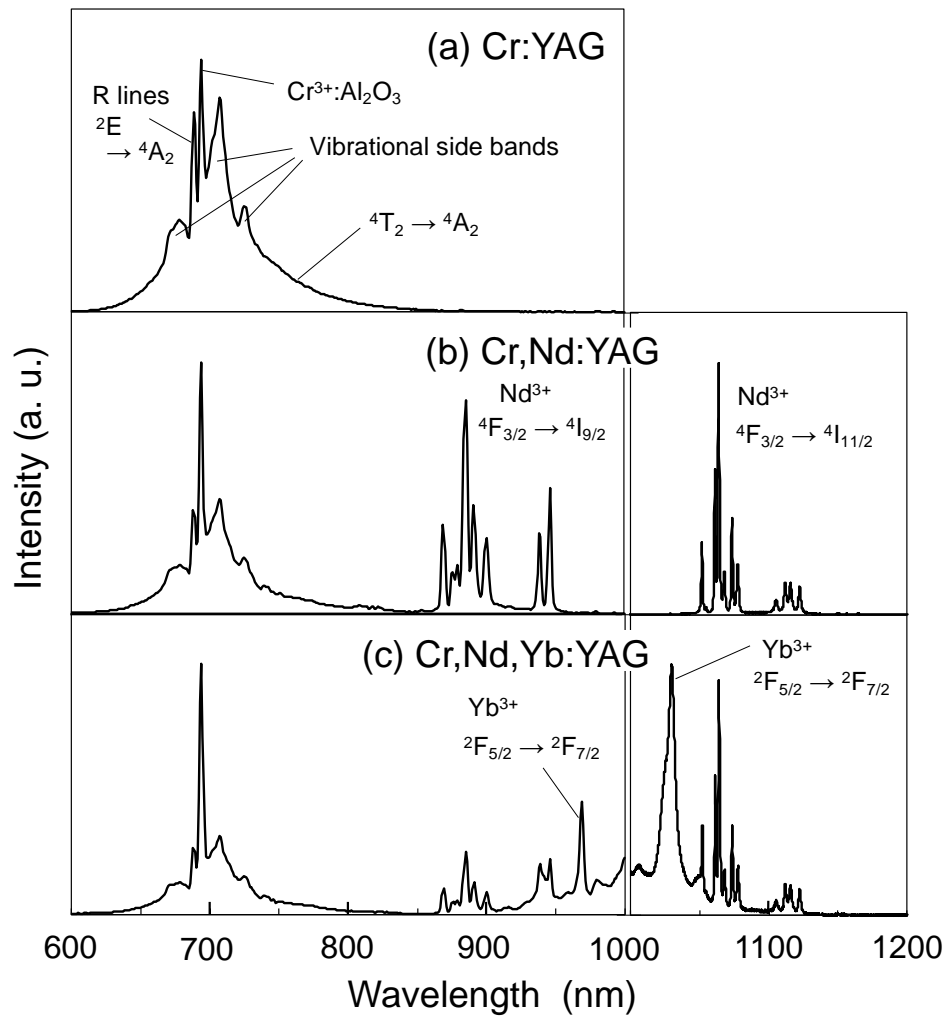
Fig. 3. Fluorescence spectra of Cr:YAG (a), Cr,Nd:YAG (b), and Cr,Nd,Yb:YAG (c) powders in a wavelength range of 600–1200 nm. The peak intensities are normalized to the same value for all the graphs. The excitation wavelength was 440–450 nm.

3. Dynamics of the ET process

3.1 Transition dynamics in Cr,Nd,Yb:YAG

The quantum cutting ET from the Cr^{3+} ions excited in the $^4T_1$ state to Yb^{3+} ions is of great interest. Although the possibility of quantum cutting has been previously reported for Cr^{3+}, Nd^{3+}, and Yb^{3+} co-doped zinc fluoroborosilicate glass [17], this effect was not significant. To clarify the evidence of quantum cutting in the YAG host material, we compared the time evolution of Yb fluorescence at 1030-nm wavelength by selective excitation of either $^4T_1$ or $^4T_2$ absorption bands of Cr,Yb:YAG powder, as shown in Fig. 4. As a result, the time histories for both the cases were almost identical, especially the rising parts, which suggests that the $Cr^{3+} \rightarrow Yb^{3+}$ quantum cutting ET is unlikely in YAG host materials.
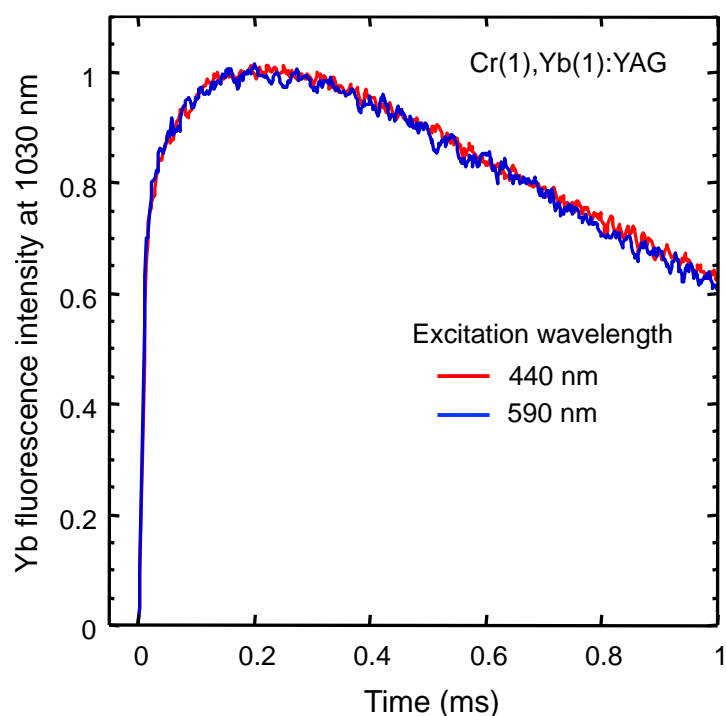

Fig. 4. Time evolution of Yb fluorescence with the excitation of $^4T_1$ or $^4T_2$ absorption bands in Cr(1),Yb(1):YAG powder.

To quantitatively understand the Yb fluorescence assisted by Cr^{3+} and Nd^{3+} ions, we investigated the transition dynamics of Cr,Nd,Yb:YAG by measuring the temporal evolution of fluorescence from these ions. The time evolutions of the number densities of the excited Cr^{3+}, Nd^{3+}, and Yb^{3+} ions [$N_{Cr}(t)$, $N_{Nd}(t)$, and $N_{Yb}(t)$] after the very fast excitation of Cr^{3+} ions are expressed by the rate equations below:

$$\frac{d}{dt}N_{Cr}(t) = -\left[\frac{1}{\tau_{Cr}} + \frac{d}{dt}P_{Cr\text{-}Nd}(t) + \frac{d}{dt}P_{Cr\text{-}Yb}(t) + \frac{d}{dt}P_{Cr\text{-}Cr}(t)\right]N_{Cr}(t),\tag{1}$$

$$\frac{d}{dt}N_{Nd}(t) = \frac{d}{dt}P_{Cr\text{-}Nd}(t)N_{Cr}(t) - \frac{1}{\tau_{Nd}}N_{Nd}(t) - \int_0^t\left[\frac{d}{d(t-t')}P_{Nd\text{-}Yb}(t-t')\right]\left[\frac{d}{dt'}P_{Cr\text{-}Nd}(t')\right]N_{Cr}(t')dt',\tag{2}$$

and

$$\frac{d}{dt}N_{Yb}(t) = \frac{d}{dt}P_{Cr\text{-}Yb}(t)N_{Cr}(t) + \int_0^t\left[\frac{d}{d(t-t')}P_{Nd\text{-}Yb}(t-t')\right]\left[\frac{d}{dt'}P_{Cr\text{-}Nd}(t')\right]N_{Cr}(t')dt' - \frac{1}{\tau_{Yb}}N_{Yb}(t),\tag{3}$$

with the initial conditions: $N_{Cr}(0)=N_0$, $N_{Nd}(0)=0$, and $N_{Yb}(0)=0$. In these equations, τ_{Cr}, τ_{Nd}, and τ_{Yb} are the lifetimes of the thermally coupled ^2E and $^4T_2$ states of Cr^{3+}, $^4F_{3/2}$ state of Nd^{3+}, and $^4F_{5/2}$ state of Yb^{3+}, respectively, in the absence of ET. $P(t)$ is the transfer function [11, 18] which describes the effects of direct ET from the donor to the acceptor. In Eqs. (1)–(3), for example, $P_{Cr\text{-}Nd}(t)$ denotes a transfer function of the ET from Cr^{3+} donors to Nd^{3+} acceptors. In Eqs. (2) and (3), the time integrations describe the cascaded ET from Cr^{3+} to Yb^{3+} via Nd^{3+} ions. At the beginning of the donor decay, $P(t)$ can be approximated by a linear function of time as

$$P(t) = Wt,\tag{4}$$

where W describes the contribution of the nearest-neighbor ET. Later, the Förster–Dexter model [19, 20] shows that $P(t)$ becomes

$$P(t) = \gamma t^{3/s}.\tag{5}$$

Here, γ is the ET parameter, and s is determined by the multipole interaction as $s = 6$, 8, and 10 for electric dipole-dipole, dipole-quadrupole, and quadrupole-quadrupole interaction mechanisms, respectively [6, 21]. As described later, $P_{Cr\text{-}Nd}(t)$, $P_{Cr\text{-}Yb}(t)$, and $P_{Nd\text{-}Yb}(t)$ are approximated as follows:

$$P_{Cr\text{-}Nd}(t) = \gamma_{Cr\text{-}Nd}t^{1/2}, P_{Cr\text{-}Yb}(t) = \gamma_{Cr\text{-}Yb}t^{1/2}, \text{ and } P_{Nd\text{-}Yb}(t) = \gamma_{Nd\text{-}Yb}t^{1/2}, \quad (6)$$

where the subscripts of γ denote the same meaning as that of $P(t)$, and γs are constants depending on the acceptor concentration. For the ET between Cr^{3+} pairs, the quadrupole-quadrupole interaction is assumed as [22]

$$P_{Cr\text{-}Cr}(t) = \gamma_{Cr\text{-}Cr}t^{3/10}. \quad (7)$$

Because all the parameters (lifetimes and ET parameters) should be independently defined, we first measured the temporal fluorescence characteristic of pure Cr:YAG at room temperature for the determination of τ_{Cr} and $\gamma_{Cr\text{-}Cr}$ by curve fitting. In the same manner, we measured Nd:YAG for τ_{Nd} and Yb:YAG for τ_{Yb}. As described in the following sections, the measured lifetimes were $\tau_{Cr} = 1.85$ ms, $\tau_{Nd} = 0.235$ ms, and $\tau_{Yb} = 0.95$ ms, respectively, and the estimated ET parameter for Cr^{3+} pairs was $\gamma_{Cr\text{-}Cr} = 0.95$ $s^{-3/10}$. Regarding other ET parameters, the decay characteristic of the Cr fluorescence of Cr,Nd:YAG was studied for the estimation of $\gamma_{Cr\text{-}Nd}$, whereas the Nd fluorescence of Nd,Yb:YAG was used for estimating $\gamma_{Nd\text{-}Yb}$. Finally, the overall performance of the ET to Yb^{3+} ($\gamma_{Cr\text{-}Nd,Yb}$) was evaluated using Cr,Nd,Yb:YAG at different Yb doping concentrations.

3.2 Fluorescence decay characteristics of donor ions and ET parameters

The temporal fluorescence decay characteristic of the donor varies depending on the presence of the acceptor, where the ET parameter can be estimated by fitting a solution to Eq. (1) or (2) for the experimental data. In this experiment, the light source of the spectrophotometer (JASCO SS-25) was switched to a Xe flash lamp to measure the time history of wavelength-resolved fluorescence excited at a selective wavelength. The overall detector system response was approximately 20 µs (full width at half maximum). For Cr,Nd:YAG, the decay curve of Cr fluorescence can be inferred from the solutions of Eq. (1) as

$$I_{Cr(Nd)}(t) = I_{Cr,0} \cdot \exp\left[-t/\tau_{Cr} - \gamma_{Cr\text{-}Cr}t^{3/10} - \gamma_{Cr\text{-}Nd}\sqrt{t}\right], \tag{8}$$

where $I_{Cr,0}$ is the fluorescence intensity immediately after the very short excitation. Here, we ignored a small sharp drop in fluorescence intensity due to the nearest-neighbor ET (W in Eq. (4)), which cannot be resolved in our experiment. The efficiency of the ET from the excited Cr^{3+} ions to Nd^{3+} ions in Cr,Nd:YAG is estimated by the following equation:

$$\eta_{Cr\text{-}Nd} = 1 - \frac{\int_0^\infty \exp\left[-\frac{t}{\tau_{Cr}} - \gamma_{Cr\text{-}Cr}t^{\frac{3}{10}} - \gamma_{Cr\text{-}Nd}\sqrt{t}\right]dt}{\int_0^\infty \exp\left[-\frac{t}{\tau_{Cr}} - \gamma_{Cr\text{-}Cr}t^{\frac{3}{10}}\right]dt}. \tag{9}$$

A similar decay curve for the Nd fluorescence of Nd,Yb:YAG with a very short pumping at 808-nm wavelength is derived as

$$I_{Nd(Yb)}(t) = I_{Nd,0} \cdot \exp\left(-t/\tau_{Nd} - \gamma_{Nd\text{-}Yb}\sqrt{t}\right). \tag{10}$$

The efficiency of ET from the excited Nd^{3+} ions to Yb^{3+} ions in Nd,Yb:YAG is expressed as:

$$\eta_{Nd\text{-}Yb} = 1 - \frac{\int_0^\infty \exp\left(-\frac{t}{\tau_{Nd}} - \gamma_{Nd\text{-}Yb}\sqrt{t}\right)dt}{\int_0^\infty \exp\left(-\frac{t}{\tau_{Nd}}\right)dt}$$

$$= \frac{\gamma_{\text{Nd-Yb}}}{2} \ \sqrt{\pi\tau_{\text{Nd}}} \ \exp\left[\left(\frac{\gamma_{\text{Nd-Yb}}}{2}\right)^2 \tau_{\text{Nd}}\right]\left[1 - \text{erf}\left(\frac{\gamma_{\text{Nd-Yb}}}{2}\sqrt{\tau_{\text{Nd}}}\right)\right]. \qquad (11)$$
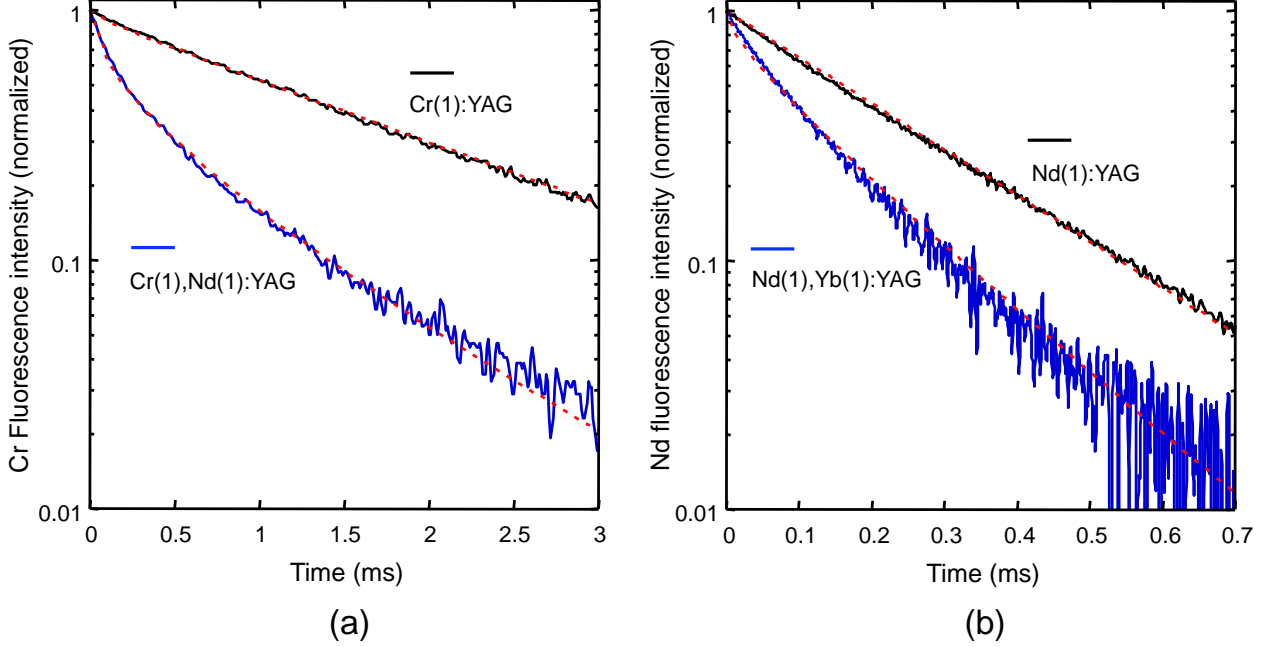

Fig. 5. Normalized temporal decay characteristics of fluorescence. (a) Cr^{3+} fluorescence at 630-nm wavelength in Cr(1):YAG and Cr(1),Nd(1):YAG powders excited at 440-nm wavelength. The red dashed lines are the curve fittings using Eq. (8). (b) Nd^{3+} fluorescence at 1064-nm wavelength in Nd(1):YAG and Nd(1),Yb(1):YAG powders excited at 808-nm wavelength. The red dashed lines are the curve fittings using Eq. (10).

The black and blue lines in Fig. 5(a) show the time histories of Cr fluorescence at 630-nm wavelength ($^4T_2 \rightarrow {^4A_2}$ transition) measured for Cr(1):YAG and Cr(1),Nd(1):YAG powders, excited by 440-nm light at room temperature. The red dashed lines correspond to the model-fitting curves obtained using Eq. (8). For Cr(1):YAG powder, the decay curve is slightly different from a single exponential function, as denoted above. From the fitting

of Eq. (8) to this data, with $\gamma_{Cr-Nd} = 0$, the lifetime and the parameter for ET in Cr pairs were estimated to be $\tau_{Cr} = 1.85$ ms and $\gamma_{Cr-Cr} = 0.95$ s$^{-3/10}$. The measured lifetime is consistent with that reported in Ref. [6]. By applying the same analysis to the data for Cr(1),Nd(1):YAG powder (blue line), we obtained $\gamma_{Cr(1)-Nd(1)} = 41.2$ s$^{-1/2}$, where the subscript [Cr(1)-Nd(1)] denotes the 1-at% doping concentrations of the Cr^{3+} and Nd^{3+} ions. Hereafter, the subscripts of γ and η have the same meaning as described previously. The ET efficiency, estimated using Eq. (9), was as high as $\eta_{Cr(1)-Nd(1)} \approx 72\%$. The black and blue lines in Fig. 5(b) show the time histories of Nd fluorescence at 1064-nm wavelength ($^4F_{3/2} \rightarrow ^4I_{11/2}$ transition) measured for the Nd(1):YAG and Nd(1),Yb(1):YAG powders, excited by 808-nm light ($^4I_{9/2} \rightarrow ^4F_{5/2}$ transition) at room temperature. The lifetime of the Nd^{3+}: $^4F_{3/2}$ level was estimated to be $\tau_{Nd} = 0.235$ ms from an exponential fitting to the decay curve for Nd(1):YAG. Using this lifetime, $\gamma_{Nd(1)-Yb(1)}$ was evaluated to be 42.5 s$^{-1/2}$ by fitting Eq. (10) to the decay curve for Nd(1),Yb(1):YAG powder (blue line in Fig. 5(b)).The ET efficiency was estimated to be $\eta_{Nd(1)-Yb(1)} \approx 41\%$ using Eq. (11). $\eta_{Cr(1)-Nd(1)}$ was higher than $\eta_{Nd(1)-Yb(1)}$, despite the reversal relation between $\gamma_{Cr(1)-Nd(1)}$ and $\gamma_{Nd(1)-Yb(1)}$, which was due to the fact that τ_{Cr} was much longer than τ_{Nd}, as is expected from Eq. (11).

To test the effect of simultaneous doping of two kinds of acceptors (Nd^{3+} and Yb^{3+}) in Cr(1),Nd(1),Yb(z):YAG, similar measurements were performed for various doping concentrations of Yb^{3+} ions. The measured fluorescence decay curves were fitted using an equation similar to Eq. (8), where γ_{Cr-Nd} was replaced by $\gamma_{Cr(1)-Nd(1),Yb(z)}$ to estimate the overall ET from Cr^{3+} to both Nd^{3+} and Yb^{3+}. Thus, the estimated $\gamma_{Cr(1)-Nd(1),Yb(z)}$ is plotted in Fig. 6, which shows a nearly linear dependence on the Yb concentration. From this data, γ_{Cr-Yb}, depending on Yb^{3+}

concentration, was inferred as $\gamma_{Cr(1)-Yb(z)} = \gamma_{Cr(1)-Nd(1),Yb(z)} - \gamma_{Cr(1)-Nd(1)}$, assuming that γ_{Cr-Nd} was independent of the Yb

concentration. In Fig. 6, the solid line corresponds to the least square fitting of the experimental data plotted by closed

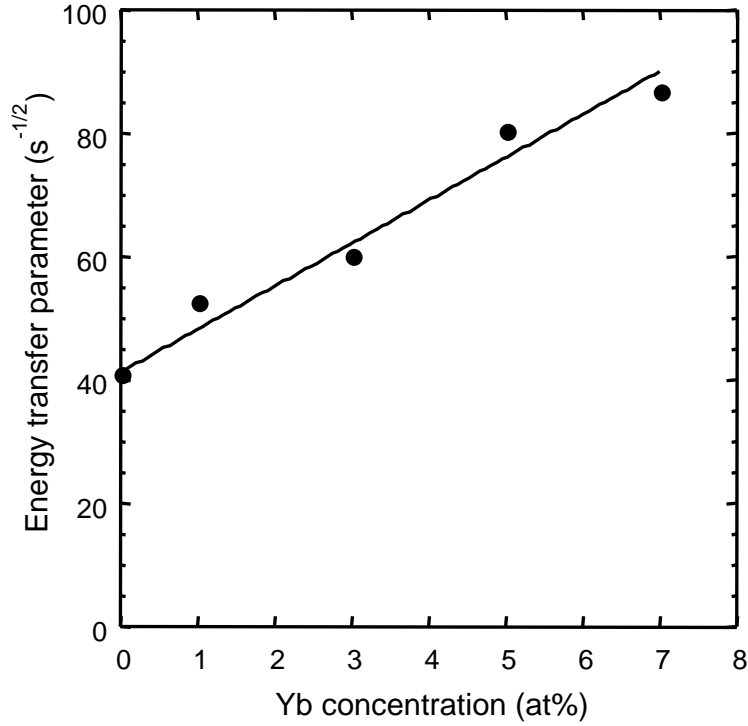circles. The overall transfer parameters for Cr(1),Nd(1),Yb(z):YAG are expressed as $\gamma_{Cr(1)-Nd(1),Yb(z)} = 6.97C_{Yb} + 41.23$.

Fig. 6. Parameters $\gamma_{Cr(1)-Nd(1),Yb(z)}$ of the overall ET from Cr^{3+} ions to Nd^{3+} and Yb^{3+} ions for Cr(1),Nd(1),Yb(z):YAG

powders. Yb concentration, z, was changed in a range of 0–7 at%. The solid line corresponds to the least square

fitting.

4. Numerical calculation of cascaded ET from Cr^{3+} to Yb^{3+} ions and enhanced near-infrared emission with an

aid of Nd^{3+} ions

To quantitatively evaluate the ET to Yb^{3+} ions, which is characterized by the time-dependent transfer rates of the

$Cr^{3+} \rightarrow Nd^{3+} \rightarrow Yb^{3+}$ cascaded process, the rate equations (Eqs. (1)–(3)) for the number densities of Cr^{3+}, Nd^{3+}, and

17

Yb^{3+} ions were numerically solved using the fourth order Runge–Kutta method with the initial conditions: $N_{Cr}(0) = 1$, $N_{Nd}(0) = 0$, and $N_{Yb}(0) = 0$. The radiative lifetime of Yb^{3+} ions, τ_{Yb}, was set to be 0.95 ms, which was measured for the Yb(1):YAG powder. The ET parameters were assumed to be $\gamma_{Cr(1)-Yb(z)} = \gamma_{Cr(1)-Nd(1),Yb(z)} - 41.2$. In this numerical calculation, the behavior of the transfer function $P(t)$ immediately after the prompt excitation of Cr^{3+} ions is unknown because of the limited time response of our measurement system. Therefore, we assumed that W in Eq. (4) obeys the equation $W(t) = W_0 \exp[-\ln(2)(t/\Delta t)^2]$, and W_0 and Δt were accordingly inferred so that the temporal variation of the calculated $N_{Nd}(t)$, especially the rising part, replicates the experimentally observed Nd fluorescence. The red line in Fig. 7(a) shows the calculated $N_{Nd}(t)$ after the excitation of the Cr^{3+} ions for Cr(1),Nd(1):YAG and was characterized by rapid growth until it peaked, followed by a relatively slow decay. This calculation result reproduces the time evolution of the Nd fluorescence plotted by open circles. In this calculation, W_0 and Δt were 1×10^4 and 20 µs, respectively. For comparison, if the nearest-neighbor transfer was not taken into account, the timing of the peak number density of $N_{Nd}(t)$ would be delayed by approximately 70 µs, and therefore, the fast buildup of Nd fluorescence would not be explained. When 1-at% Yb^{3+} ions were co-doped into Cr(1),Nd(1):YAG, the fluorescence intensity, shown by open squares in Fig. 7(a), reached its peak earlier than the case without Yb^{3+} doping (open circles), which suggests the fast cascaded ET from Cr^{3+} to Yb^{3+} ions via Nd^{3+} ions. This time behavior of Nd fluorescence was predicted well by the calculation result shown by the blue line in Fig. 7(a). Figure 7(b) shows a comparison between the experimentally observed time history of Yb fluorescence (closed circles) with the corresponding calculation result of Yb^{3+} number density ($N_{Yb}(t)$). Both time evolution features agreed well with each other. Therefore, numerical

calculations predicted the physical processes in Cr and Nd co-doped Yb:YAG materials. The contribution of the nearest-neighbor process can be ignored for the secondary process of $Nd^{3+} \rightarrow Yb^{3+}$ ET, because the buildup of the number density of excited Nd^{3+} ions is a gradual process. For the $Cr^{3+} \rightarrow Yb^{3+}$ ET, the contribution of the nearest-neighbor process is minor because γ_{Cr-Yb} is smaller than γ_{Cr-Nd}.
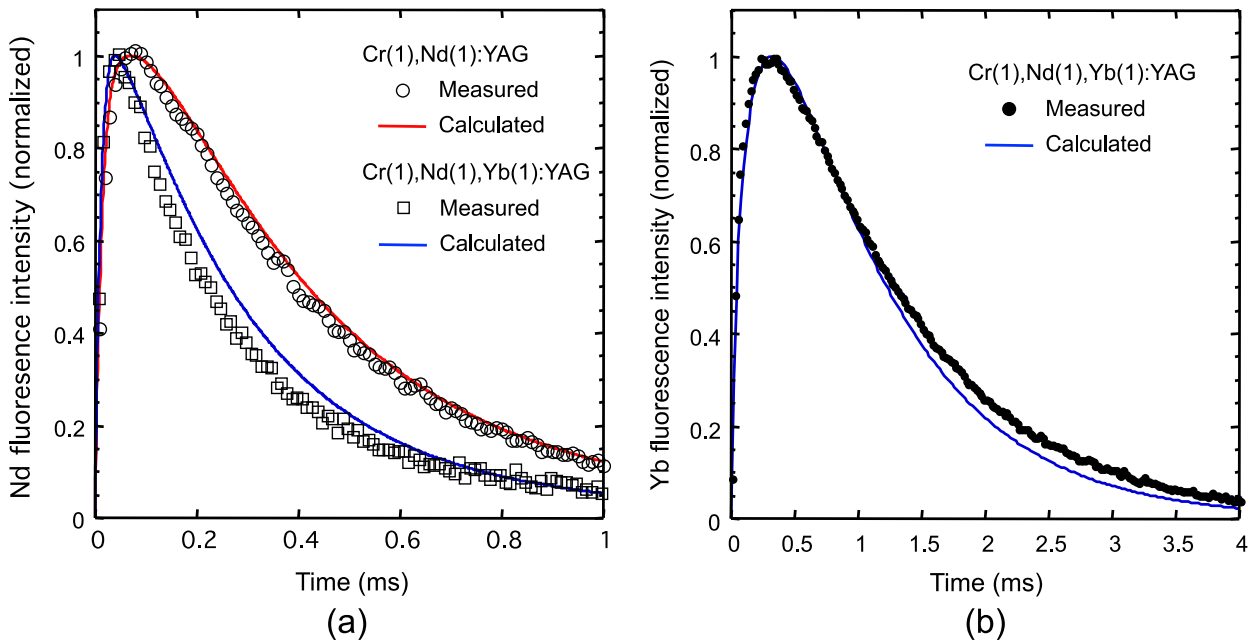

Fig. 7. Experimentally observed time histories of Nd fluorescence (1064 nm) and Yb fluorescence (1030 nm) were compared with the calculated temporal characteristics of the Nd and Yb number densities. (a) Normalized temporal evolutions of Nd fluorescence for Cr(1),Nd(1):YAG (open circles) and Cr(1),Nd(1),Yb(1):YAG (open squares). Red and blue lines correspond to the calculation results of the normalized $N_{Nd}(t)$. (b) Normalized temporal evolutions of Yb fluorescence for Cr(1),Nd(1),Yb(1):YAG (closed circles). The blue line corresponds to the normalized $N_{Yb}(t)$.

Based on the calculation benchmarking described above, we estimated the efficiency of Yb fluorescence, which would be sensitized by the direct $Cr^{3+} \rightarrow Yb^{3+}$ ET and cascaded $Cr^{3+} \rightarrow Nd^{3+} \rightarrow Yb^{3+}$ ET in the Cr,Nd,Yb:YAG. In the following calculation, the doping concentrations of the Cr^{3+} and Nd^{3+} ions were fixed at 1 at%, and that of Yb^{3+} was varied in the range of 0–7 at%. To depict the effect of the doping concentration of the Yb^{3+} ions, we compared the temporal changes in $N_{Cr}(t)$, $N_{Nd}(t)$, and $N_{Yb}(t)$ for Cr(1),Nd(1),Yb(1):YAG and Cr(1),Nd(1),Yb(3):YAG, as shown in Fig. 8. In the case of Cr(1),Nd(1),Yb(1):YAG (dashed lines), $N_{Cr}(t)$ rapidly decreases compared with the exponential decay with τ_{Cr} (1.85 ms), and then $N_{Cr}(t)$ rapidly increases to its maximum, followed by decay due to the ET to Yb^{3+} ions. When the Yb concentration is increased to 3 at% (solid lines in Fig. 8), the decay speed of $N_{Cr}(t)$ becomes slightly faster, while the changes in $N_{Nd}(t)$ and $N_{Yb}(t)$ are significant. It can be clearly seen that the growth of $N_{Nd}(t)$ is strongly suppressed, whereas $N_{Yb}(t)$ is enhanced by a factor of approximately 2 compared with that of Cr(1),Nd(1),Yb(1):YAG.
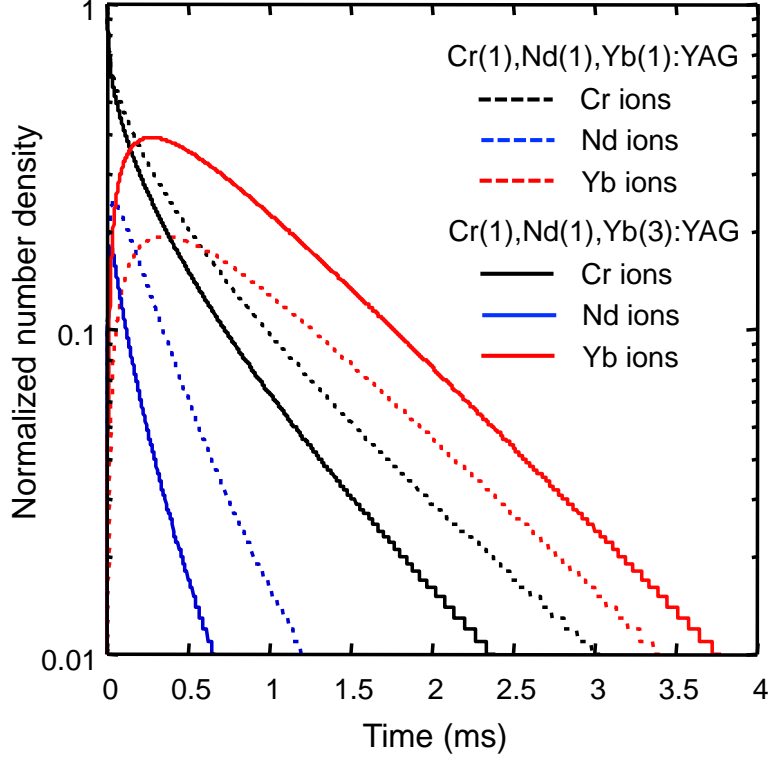
Fig. 8. Typical calculated time evolutions of the number densities of the Cr^{3+}, Nd^{3+} and Yb^{3+} ions for

Cr(1),Nd(1),Yb(1):YAG and Cr(1),Nd(1),Yb(3):YAG.

Figure 9 shows the balance of the quantum yield of fluorescence (Q_{Cr}, Q_{Nd}, and Q_{Yb}) for

Cr(1),Nd(1),Yb(z):YAG. Q_{Nd} and Q_{Yb} are defined as $Q_{Nd} = \int_0^\infty [N_{Nd}(t)/\tau_{Nd}]dt$ and $Q_{Yb} = \int_0^\infty [N_{Yb}(t)/\tau_{Yb}]dt$,

respectively, for the Nd^{3+} and Yb^{3+} ions. Q_{Cr} is estimated as $1 - (Q_{Nd} + Q_{Yb})$. In the case without Yb doping, Q_{Nd}

exceeds 70%, as expected from Fig. 5(a), which is consistent with the analysis done using Eq. (9). When 1-at%

Yb^{3+} ions are doped, Q_{Yb} is ~35% with a decrease in Q_{Nd} from ~70% to ~40%. Thus, Q_{Nd} decreases with increasing

Yb concentration, whereas Q_{Yb} increases. Q_{Yb} reaches a very high value of more than 80% for C_{Yb} of 7 at%. To

elucidate the effectiveness of the cascaded $Cr^{3+} \rightarrow Nd^{3+} \rightarrow Yb^{3+}$ ET, the Q_{Yb} values calculated for Cr(1)Yb(z):YAG

are also plotted by red open squares in Fig. 9. The differences between Q_{Yb}s with and without the co-doping of Nd^{3+} ions are attributed to the cascaded ET process, which increases the Q_{Yb} by 10–20% depending on the Yb concentration.
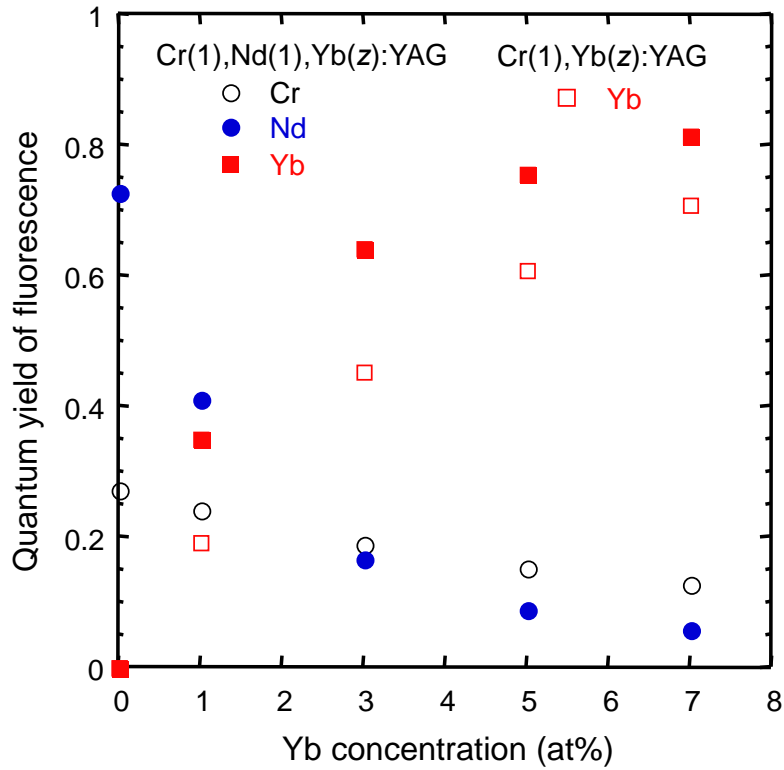

Fig. 9. Calculated quantum yield balance corresponding to the Yb concentration of Cr(1),Nd(1),Yb(z):YAG.

5. Conclusions

The excitation spectrum of Cr,Nd,Yb:YAG has many wide bands, which coincide with the absorption bands of Cr^{3+}, Nd^{3+}, and Yb^{3+} ions, in the wavelength range of 400–1000 nm. To understand this feature of the excitation spectrum, especially the contribution of the wide spectral components in the visible wavelength range originating from Cr^{3+} ions, we extensively studied the ET processes in the triply doped Cr,Nd,Yb:YAG and doubly doped

Cr,Nd:YAG and Nd,Yb:YAG. This process was explained well by the dipole-dipole interaction model between the donor and acceptor ions, while the quantum cutting process from the Cr^{3+}:$^4T_1$ state was unlikely for the excitation of Yb^{3+} ions. The ET parameters for doubly doped YAGs were estimated to be $\gamma_{Cr(1)-Nd(1)} = 41.2$ s$^{-1/2}$ and $\gamma_{Nd(1)-Yb(1)} = 42.5$ s$^{-1/2}$ for Cr(1)Nd(1):YAG and Nd(1)Yb(1):YAG, respectively. The corresponding ET efficiencies for the former and latter materials were 72% and 41%, respectively. The overall ET parameters, including donor-acceptor combinations of Cr^{3+}-Nd^{3+} and C^{r3+}-Yb^{3+} for Cr,Nd,Yb:YAG, increased linearly with increasing Yb concentration. Using the estimated ET parameters, the rate equations for the number densities of the excited states of Cr^{3+}, Nd^{3+}, and Yb^{3+} ions were numerically solved, showing good benchmarking results for predicting the temporal behavior of fluorescence intensity for Nd^{3+} and Yb^{3+} ions. The quantum yield of Yb fluorescence in Cr,Nd,Yb:YAG with the excitation of Cr^{3+} ions was enhanced by the cascaded $Cr^{3+} \rightarrow Nd^{3+} \rightarrow Yb^{3+}$ ET, which was assisted by the co-doping of Nd^{3+} ions with only 1-at% content, and the estimated quantum yield was 35–81% for Yb concentrations of 1–7 at%. Therefore, Cr,Nd,Yb:YAG is a very useful material for light emission at ~1000-nm wavelength by pumping with visible light, and it would be a promising material for applications in crystalline Si photovoltaic cells and solar-pumped short-pulse lasers.

References

[1] T. Saiki, K. Imasaki, S. Motokoshi, C. Yamanaka, H. Fujita, M. Nakatsuka, Y. Izawa, "Disk-type Nd/Cr:YAG ceramic lasers pumped by arc-metal-halide-lamp," Opt. Commun. **268** (2006) 155–159, https://doi.org/10.1016/j.optcom.2006.07.002.

[2] K. Fujioka, T. Saiki, S. Motokoshi, Y. Fujimoto, H. Fujita, M. Nakatsuka, "Luminescence properties of highly Cr co-doped Nd:YAG powder produced by sol–gel method," J. Lum. **130** (2010) 455–459, https://doi.org/10.1016/j.jlumin.2009.10.012.

[3] M. Yamaga , Y. Oda , H. Uno, K. Hasegawa , H. Ito , and S. Mizuno, "Formation probability of Cr-Nd pair and energy transfer from Cr to Nd in $Y_3Al_5O_{12}$ ceramics codoped with Nd and Cr," J. Appl. Phys. **112** (2012) 063508, https://doi.org/10.1063/1.4752403.

[4] Y. Honda, S. Motokoshi, T. Jitsuno, N. Miyanaga, K. Fujioka, M. Nakatsuka, M. Yoshida, "Temperature dependence of optical properties in Nd/Cr:YAG materials," J. Lumin. **148** (2014) 342-346, https://doi.org/10.1016/j.jlumin.2013.12.044.

[5] Y. Honda, S. Motokoshi, T. Jitsuno, K. Fujioka, M. Nakatsuka, M. Yoshida, T. Yamada, J. Kawanaka and N. Miyanaga, "Temperature-dependent fluorescence decay and energy transfer in Nd/Cr:YAG ceramics," Opt. Mater. **90** (2019) 215–219, https://doi.org/10.1016/j.optmat.2019.02.032.

[6] P. Hong, X. X. Zhang, C. W. Struck, B. Di Bartolo, "Luminescence of Cr^{3+} and energy transfer between Cr^{3+} and Nd^{3+} ions in yttrium aluminum garnet," J. Appl. Phys. **78** (1995) 4659–4667, https://doi.org/10.1063/1.359813.

[7] V. Lupei, A. Lupei, C. Gheorghe, and A. Ikesue, "Spectroscopic and de-excitation properties of (Cr,Nd):YAG transparent ceramics," Opt. Mater. Exp. **6** (2016) 552-557, https://doi.org/10.1364/OME.6.000552.

[8] V. Lupei, A. Lupei A. Ikesue, C. Gheorghe, S. Hau, "Sensitization of Yb^{3+} emission in laser oxide ceramics," Romanian Reports in Physics, 62 (2010) 429–443, http://rrp.nipne.ro/2010_62_3/Art%201%20VLupei.pdf.

[9] S. Ye, J. Zhou, S. Wang, R. Hu, D. Wang, and J. Qiu, "Broadband downshifting luminescence in Cr^{3+}-Yb^{3+} codoped garnet for efficient photovoltaic generation," Opt. Exp. **21** (2013) 4167-4173, https://doi.org/10.1364/OE.21.004167.

[10] K. Fujioka, T. Saiki, S. Motokoshi, Y. Fujimoto, H. Fujita, M. Nakatsuka, "Parameter mapping survey on optimized sensitizing effect of Ce/Cr/Nd: YAG material for solar-pumped solid-state lasers," J. Lum. **143** (2013) 10-13, https://doi.org/10.1016/j.jlumin.2013.04.040.

[11] V. Lupei, A. Lupei, C. Gheorghe, A. Ikesue, "Emission sensitization processes involving Nd^{3+} in YAG," J. Lum. **170** (2016) 594–601, https://doi.org/10.1016/j.jlumin.2015.04.045.

[12] K. Fujioka, T. Saiki, S. Motokoshi, Y. Fujimoto, H. Fujita, and M. Nakatsuka, "Pre-evaluation method for the spectroscopic properties of YAG bulk materials by sol-gel synthetic YAG powder," Ceram. Int. **35** (2009) 2393–2399, https://doi.org/10.1016/j.ceramint.2009.02.010.

[13] International Center for Diffraction Data (ICDD) Card #33-0040.

[14] D. C. Brown, "Heat, fluorescence, and ftimulated-emission power densities and fractions in Nd:YAG," IEEE J. Quantum Electron. **34 (**1998) 560-572, https://doi.org/10.1109/3.661467.

[15] K. M. Kinsman, J. McKittrick, E. Sluzky and K. Hesse, "Phase Development and Luminescence in Chromium-Doped Yttrium Aluminum Garnet (YAC:Cr) Phosphors," J. Am. Ceram. Soc, **77** (1994) 2866–2872, https://doi.org/10.1111/j.1151-2916.1994.tb04516.x

[16] L. E. Shea, J. McKittrick, and O. A. Lopez, "Synthesis of Red-Emitting, Small Particle Size Luminescent Oxides Using an Optimized Combustion Process," J. Am. Ceram. Soc. **79** (1996) 3257-65, https://doi.org/10.1111/j.1151-2916.1996.tb08103.x

[17] D. Ghosh, S. Balaji, K. Biswas and K. Annapurna, "Quantum cutting induced multifold enhanced emission from Cr^{3+}-Yb^{3+}-Nd^{3+} doped zinc fluoroboro silicate glass - Role of host material," J. Appl. Phys. **120** (2016) 233104, https://doi.org/10.1063/1.4971979.

[18] V. Lupei, A. Lupei, C. Gheorghe, I. Urrsu, "Effect of nearest-neighbor pairs on the energy transfer in Nd:YAG," Appl. Phys. Lett. **59** (1991) 905-907, https://doi.org/10.1063/1.106420.

[19] T. Förster, "Zwischenmolekulare energiewanderrung und fluoreszenz," Annalen der Physik **437**(2) (1948) 55-75, http://dx.doi.org/10.1002/andp.19484370105, https://onlinelibrary.wiley.com/doi/pdfdirect/10.1002/andp.19484370105.

[20] D. L. Dexter, "A Theory of Sensitized Luminescence in Solids," J. Chem. Phys. **21** (1953) 836–850,

https://doi.org/10.1063/1.1699044.

[21] M. Inokuti and F. Hirayama, "Influence of energy transfer by the exchange mechanism on donor luminescence,"

J. Chem. Phys. 43 (1965) 1978-1989, https://doi.org/10.1063/1.1697063.

[22] G. F. Imbusch, "Energy transfer in ruby," Phys. Rev. **153** (1967) 326–337,

https://doi.org/10.1103/PhysRev.153.326.

Figure captions

Fig. 1. Schematic illustration of the energy level diagrams of the Cr^{3+}, Nd^{3+} and Yb^{3+} ions. Thick arrows

denote the possible energy transfer (ET) and the quantum cutting processes between the different

ion species.

Fig. 2. Excitation spectra of 1030-nm Yb emission for Cr,Yb:YAG powder (black line) and Cr,Nd,Yb:YAG

powder (blue and red lines). The solar spectrum (AM 1.5, dotted green line) is shown for reference.

Fig. 3. Fluorescence spectra of Cr:YAG (a), Cr,Nd:YAG (b), and Cr,Nd,Yb:YAG (c) powders in a

wavelength range of 600–1200 nm. The peak intensities are normalized to the same value for all the

graphs. The excitation wavelength was 440–450 nm.

Fig. 4. Time evolution of Yb fluorescence with the excitation of $^4T_1$ or $^4T_2$ absorption bands in

Cr(1),Yb(1):YAG powder.

Fig. 5. Normalized temporal decay characteristics of fluorescence. (a) Cr^{3+} fluorescence at 630-nm

wavelength in Cr(1):YAG and Cr(1),Nd(1):YAG powders excited at 440-nm wavelength. The red

dashed lines are the curve fittings using Eq. (8). (b) Nd^{3+} fluorescence at 1064-nm wavelength in

Nd(1):YAG and Nd(1),Yb(1):YAG powders excited at 808-nm wavelength. The red dashed lines

are the curve fittings using Eq. (10).

Fig. 6. Parameters $\gamma_{Cr(1)-Nd(1),Yb(z)}$ of the overall ET from Cr^{3+} ions to Nd^{3+} and Yb^{3+} ions for

Cr(1),Nd(1),Yb(z):YAG powders. Yb concentration, z, was changed in a range of 0–7 at%. The

solid line corresponds to the least square fitting.

Fig. 7. Experimentally observed time histories of Nd fluorescence (1064 nm) and Yb fluorescence

(1030 nm) were compared with the calculated temporal characteristics of the Nd and Yb number

densities. (a) Normalized temporal evolutions of Nd fluorescence for Cr(1),Nd(1):YAG (open

circles) and Cr(1),Nd(1),Yb(1):YAG (open squares). Red and blue lines correspond to the

calculation results of the normalized $N_{Nd}(t)$. (b) Normalized temporal evolutions of Yb fluorescence

for Cr(1),Nd(1),Yb(1):YAG (closed circles). The blue line corresponds to the normalized $N_{Yb}(t)$.

Fig. 8. Typical calculated time evolutions of the number densities of the Cr^{3+}, Nd^{3+} and Yb^{3+} ions for

Cr(1),Nd(1),Yb(1):YAG and Cr(1),Nd(1),Yb(3):YAG.

Fig. 9. Calculated quantum yield balance corresponding to the Yb concentration of

Cr(1),Nd(1),Yb(z):YAG.